Ge–Sb–S–Se–Te amorphous chalcogenide thin films towards on-chip nonlinear photonic devices

J.-B. Dory, C. Castro-Chavarria, A. Verdy, J.-B. Jager, M. Bernard, C. Sabbione, M. Tessaire, J.-M. Fedeli, A. Coillet, B. Cluzel, et al.

▶ **To cite this version:**

J.-B. Dory, C. Castro-Chavarria, A. Verdy, J.-B. Jager, M. Bernard, et al.. Ge–Sb–S–Se–Te amorphous chalcogenide thin films towards on-chip nonlinear photonic devices. Scientific Reports, 2020, 10, pp.11894. 10.1038/s41598-020-67377-9 . cea-02903381

HAL Id: cea-02903381
https://cea.hal.science/cea-02903381

Submitted on 3 Jun 2021

HAL is a multi-disciplinary open access archive for the deposit and dissemination of scientific research documents, whether they are published or not. The documents may come from teaching and research institutions in France or abroad, or from public or private research centers.

L'archive ouverte pluridisciplinaire **HAL**, est destinée au dépôt et à la diffusion de documents scientifiques de niveau recherche, publiés ou non, émanant des établissements d'enseignement et de recherche français ou étrangers, des laboratoires publics ou privés.

Distributed under a Creative Commons Attribution 4.0 International License

SCIENTIFIC REPORTS
nature research

Check for updates

OPEN

Ge–Sb–S–Se–Te amorphous chalcogenide thin films towards on-chip nonlinear photonic devices

J.-B. Dory[1], C. Castro-Chavarria[1], A. Verdy[1], J.-B. Jager[2], M. Bernard[1], C. Sabbione[1], M. Tessaire[1], J.-M. Fédéli[1], A. Coillet[3], B. Cluzel[3] & P. Noé[1]✉

Thanks to their unique optical properties Ge–Sb–S–Se–Te amorphous chalcogenide materials and compounds offer tremendous opportunities of applications, in particular in near and mid-infrared range. This spectral range is for instance of high interest for photonics or optical sensors. Using co-sputtering technique of chalcogenide compound targets in a 200 mm industrial deposition tool, we show how by modifying the amorphous structure of $GeSb_wS_xSe_yTe_z$ chalcogenide thin films one can significantly tailor their linear and nonlinear optical properties. Modelling of spectroscopic ellipsometry data collected on the as-deposited chalcogenide thin films is used to evaluate their linear and nonlinear properties. Moreover, Raman and Fourier-transform infrared spectroscopies permitted to get a description of their amorphous structure. For the purpose of applications, their thermal stability upon annealing is also evaluated. We demonstrate that depending on the $GeSb_wS_xSe_yTe_z$ film composition a trade-off between a high transparency in near- or mid-infrared ranges, strong nonlinearity and good thermal stability can be found in order to use such materials for applications compatible with the standard CMOS integration processes of microelectronics and photonics.

Chalcogenides are commonly defined as non-oxide compounds containing at least one chalcogen element such as S, Se and/or Te (belonging to group 16 of O) alloyed with electropositive elements (more often elements of group 15 (As, Sb, Bi) and/or group 14 (Si, Ge, Sn, Pb)). Chalcogenide exhibit a unique portfolio of properties which has led to their wide use for non-volatile memory applications such as optical data storage (CD-RW and DVD-RAM), Conductive-Bridging Random Access Memory or Phase-Change Random Access Memory[1]. More recently, thanks to the huge electronic nonlinearities and discontinuity [in particular the Ovonic Threshold Switching (OTS) mechanism] observed in some chalcogenide glasses (CGs) under electrical field application, the latter are considered as the most promising materials to be used as innovative selector element in 3D memory arrays[2,3]. Besides, thanks to a high transparency window in the infrared range and large optical nonlinearities[4,5], chalcogenide glasses offer also opportunities for elaboration of innovative mid-infrared (MIR) components such as MIR super-continuum (SC) laser sources, optical sensors, IR micro-lens arrays and all-optical integrated circuits[6,7]. The potential of amorphous semiconductors for optical applications is already demonstrated but the progresses in glass science is still behind crystal science due to inherent complexity of highly disordered systems hindering thus their structural description and theoretical modelling[8]. Up to now, state-of-the-art of MIR SC generation have been achieved by using mainly chalcogenide compounds containing Arsenic such as As_2S_3 and As_2Se_3 fibres[9,10] or GeAsSe rib waveguides[11]. However, the R.E.A.C.H. European recommendation (https://echa.europa.eu/regulations/reach) as well as a recent publication from the World Health Organization (https://www.who.int/ipcs/assessment/public_health/chemicals_phc/en/) have both identified Arsenic as one of the ten most harmful chemicals for human health. As a result, developing new materials using less and less harmful or rare element is a huge challenge for the materials science.

In that context, the aim of the present study is to develop As-free amorphous chalcogenide thin films compatible with CMOS technology of microelectronics and photonics. The ultimate purpose would be to give clear clues to select the most suitable chalcogenide compositions exhibiting the best trade-off between stability and optical properties in order to enable future achievement of passive and active on-chip MIR components such

[1]Université Grenoble Alpes, CEA, LETI, MINATEC Campus, 17 Avenue des Martyrs, 38000 Grenoble, France. [2]Université Grenoble Alpes, CEA, IRIG, MINATEC Campus, 17 Avenue des Martyrs, 38000 Grenoble, France. [3]ICB, UMR CNRS 6303, Université de Bourgogne Franche Comté, 9, Avenue Alain-Savary, BP 47870, 21078 Dijon cedex, France. ✉email: pierre.noe@cea.fr

as MIR optical waveguides or portable SC laser sources. To this aim, a wide composition range of amorphous $GeSb_wS_xSe_yTe_z$ chalcogenide thin films were deposited on 200 mm Si-based substrates by means of magnetron co-sputtering technique. Despite the ability of such technique to permit a fast and easy study of a wide range of chalcogenide thin films' compositions, only very few studies of the optical properties of co-sputtered chalcogenide films have been reported in literature yet[12–14]. Since the local structure of glasses determines their physical properties, a first description of the amorphous structure of the (co-)sputtered chalcogenide films was probed by means of Raman and Fourier-transform infrared (FTIR) spectroscopies. Then, modelling of the spectroscopic ellipsometry data acquired on as-deposited thin films permits to determine their linear optical constants in the visible to near infrared range. From these experimental data and by using the well-known Sheik–Bahae model, a first evaluation of their n_2 Kerr refractive index is given in order to get better insight on their nonlinear optical properties. Moreover, the thermal stability of all deposited thin films was probed by monitoring their optical reflectivity during annealing under N_2 atmosphere. Finally, some of the $GeSb_wS_xSe_yTe_z$ compositions are shown to exhibit an optimized compromise between the good glass stability (but limited transparency window) of S-based chalcogenide and the high 3rd order nonlinear refractive index n_2 (but low thermal stability of the amorphous phase) of Te-based compositions[15,16]. Besides, we reveal the major impact of Sb introduction in GeS_x and $GeSe_x$ binary as well as GeS_xSe_y and $GeSe_xTe_y$ ternary compounds on the amorphous structure and therefore on the optical properties of chalcogenide thin films obtained by co-sputtering deposition technique.

Methods

Chalcogenide thin films deposition and basic characterization. The amorphous chalcogenide thin films were obtained by means of (co-)sputtering on 200 mm Si(001) substrates from either a single or up to simultaneously three targets of pure chalcogenide compounds. Before (co-)sputtering deposition, we did not perform any particular surface preparation of the Si substrates. Indeed, the substrates are standard high-quality microelectronic Si wafers with high purity and very low surface contamination and covered, as usual, by a few nm thick thin layer of native silicon oxide. The films' thicknesses were either fixed to 100 nm or 200 nm. The compositions of sputtering targets were $Ge_{40}S_{60}$, $Ge_{37}S_{63}$, $Ge_{26}Se_{74}$, $Ge_{30}Se_{70}$, $Ge_{52}Te_{48}$, pure Sb and pure Ge. The targets were sputtered by magnetron sputtering with an Ar plasma either achieved by using radio frequency (RF) at 13.56 MHz or direct courant (DC) plasma discharges. It is well known that deposition parameters of magnetron sputtering technique, such as Argon gas flow, substrate temperature, deposition vessel geometry, RF or DC plasma, applied power on targets and deposition pressure especially can play a major role on the density, composition and structure of the thin films[17–19]. In this study, all deposition were made using the same Ar flow and the deposition pressure was kept at 5.10^{-3} mBar. Note that due to geometry and deposition conditions in our multi-cathode chamber, the substrate temperature was kept very close to room temperature during deposition of chalcogenide films.

The different compositions of the sputtered films were obtained by varying the power applied to the targets between 10 and 220 W (see Sect. 1 of the Supplementary Information). Note that a slight composition deviation between targets and deposited films can occur. This is the result of the different sputtering yields between chemical elements due to a selective atoms-ions interactions. This effect also depends on the deposition conditions such as applied power or aging of the targets. For instance, $Ge_{38}S_{62}$ and $Ge_{36}S_{64}$ thin film samples were obtained by means of sputtering of the same $Ge_{37}S_{63}$ target and in the same deposition conditions. The slight deviation of composition is probably due to aging of the target after a high number of deposition cycles. This variation is of the order of the accuracy level of characterization methods used to determine films' compositions (~ 1 at. %). However, this trend on compositions is also confirmed by changes of properties and amorphous structure of these films as shown in the following.

The different compositions of the films were adjusted by varying the deposition rates ratio in between the different sputtering targets during the co-sputtering deposition. Then, the obtained compositions were verified by means of Wavelength Dispersive X-Ray Fluorescence (WDXRF) and/or ion beam analysis (Rutherford Back Scattering (RBS) and Particle Induced X-Ray Emission (PIXE) measurements).

Immediately after deposition all films were transferred under high vacuum in a second deposition chamber in order to be capped by a 10 nm thick SiN_x protective layer. This nitride layer deposited by reactive RF magnetron sputtering of a pure Si target under Ar/N_2 reactive atmosphere is shown to be highly efficient to protect chalcogenide thin films from surface oxidation since chalcogenides are particularly prone to oxidation[18,20,21]. We must note that during SiN_x deposition the temperature of the chalcogenide thin film samples can reach up to 180 °C due to thermal heating resulting from RF sputtering of the Si target. We note that since this temperature is below the glass transition temperature of our chalcogenide samples, it is expected to have no detrimental impact on the films, as already studied for similar chalcogenide bulk glasses and thin films[4,22–27].

In order to get a first evaluation of the limit of stability of the deposited amorphous chalcogenides upon annealing, the reflectivity of the films at 670 nm was monitored during an annealing under N_2 atmosphere. The heating ramp rate was fixed to 10 °C/min. The limit temperature was defined as the temperature for which an irreversible change of sample reflectivity was detected indicating an irreversible structural modification of the amorphous material (phase crystallization, phase segregation, layer delamination …).

FTIR and Raman scattering measurements. Fourier-Transform Infrared spectroscopy (FTIR) analysis of local order of the amorphous films was performed in transmission mode in the 100–500 cm^{-1} range. All absorbance spectra were acquired in the same experimental conditions (average over 32 scans and spectral resolution of 2 cm^{-1}). A reference absorbance spectrum collected on a Si(100) substrate covered by a 10 nm SiN_x capping layer was used as background subtraction for all FTIR spectra acquired on the chalcogenide thin

film samples. Then, all raw spectra were normalized to the chalcogenide film thicknesses in order to get a more accurate comparison between the different thin film samples.

Raman scattering spectra were acquired in a micro-Raman spectrometer in the range from 100 to 500 cm^{-1} using a laser probe at 532 nm wavelength. The acquisition conditions (laser power, magnification and exposure time) were adjusted for each films in order to optimize the signal-to-noise ratio but with a particular emphasis to keep no or very limited impact on the material's structure.

Spectroscopic ellipsometry measurements. Spectroscopic ellipsometry (SE) measurements were performed in the 400–1,700 nm range. Data were collected at three incidence angles (55, 65 and 75°). Analysis of the raw data was performed using WVASE 32® software. A 10 nm SiN_x layer deposited on a Si substrate was also measured separately in order to take into account any possible influence of capping layer when modelling of chalcogenide films' data. For chalcogenide thin film samples, the film thicknesses, dielectric functions, optical constants (refractive index n and extinction coefficient k) and absorption coefficient α as a function of the photon energy in the 0.73–3.1 eV range were obtained by means of modelling of the SE data with a Cody-Lorentz (CL) model (see also Sect. 3 of the Supplementary Information).

The optical bandgaps of the films were estimated by using the bandgap values obtained from the CL fitting model (E_g^{CL}) as well as by considering the energy for which the absorption reaches 10^4 cm^{-1} (E_g^{04}).

Using the M-line technique[28] at two wavelengths (1,313 and 1,548 nm), the effective refractive indices of the films as well as their thicknesses (by prism coupling technic) were also accurately determined (not shown). The obtained values of n at 1,313 and 1,548 nm were compared with those obtained from SE modelling and were used to validate the accuracy of SE results.

In order to get an estimation of the optical nonlinearities of the studied glasses the well-known Sheik–Bahae model was used[29]. This method allows to estimate nonlinear Kerr refractive index n_2 by means of an analytical approach using linear refractive index and optical band gap energy values. This model takes into account contributions from several physical origins: two-photon and Raman transitions, linear Stark and quadratic Stark effects. A divergent term is also added in order to subtract the unphysical behaviour resulting from the formula used to adjust these contributions. For these calculations, we used a Sellmeier fit of the refractive index in the material's transparency range obtained by using the Cody-Lorentz modelling and the optical band gap energy E_g^{04}. The results of Sellmeier fits were extrapolated to wavelengths beyond spectral range of the ellipsometry measurements.

Results and discussion

As-deposited chalcogenide thin films' composition map. All compositions of the studied chalcogenide thin films are reported on the ternary diagrams of Fig. 1 (see also Sect. 1 of the Supplementary Information). As shown in Fig. 1 the wide composition range of amorphous chalcogenide thin films that can be obtained exhibits a minimal thermal stability of 250 °C and up to higher than 400 °C depending on film composition (see "Methods" and Sect. 2 of the Supplementary Information).

Amorphous structure of chalcogenide thin films by FTIR and Raman spectroscopies. A summary of the bonds nature and main structural motifs detected in the amorphous structure of chalcogenide thin films deposited by co-sputtering is listed hereafter. All the details are given in Sect. 3 of the Supplementary Information. Table 1 summarizes the main structural motifs for each type of chalcogenide thin film compounds of the present study deduced from analysis of the Raman and FTIR vibration modes as well as the references from literature supporting our conclusions. As follows, the main conclusions on the amorphous structure drawn from the analysis of the Raman and FTIR spectra of each film is summarized system by system based on the extended discussion of the Supplementary Information.

$Ge_{1-x}Se_x$, $Ge_{1-x}S_x$ and $[Ge_{40}S_{60}]_{1-x}[Ge_{26}Se_{74}]_x$ thin films. In Fig. 2a are shown the FTIR and Raman spectra acquired on the $Ge_{1-x}Se_x$, thin films, with x varying in 0.63–0.74 range. Se enrichment in $Ge_{1-x}Se_x$ films leads to reduction of homopolar inter-tetrahedral Ge–Ge bonds (Ge-Ge_{ETH}) in favour of Se–Se ones accompanied by an increase of the number of corner-sharing (CS) compared with edge-sharing (ES) $GeSe_{4/2}$ tetrahedra in excellent agreement with previous works[30].

The FTIR and Raman spectra of $Ge_{1-x}S_x$ films are presented in Fig. 2b. In amorphous $Ge_{1-x}S_x$ films, vibrational modes corresponding to $GeS_{4/2}$ tetrahedra are observed along with contributions attributed to Ge–Ge and S–S homopolar bonds. The decrease of disorder in the amorphous $Ge_{1-x}S_x$ films evidenced by a hardening of the Raman modes is observed when going from $Ge_{40}S_{60}$ toward $Ge_{36}S_{64}$ composition as the amorphous network evolves toward composition being more and more close to that of the stoichiometric GeS_2 glass. The intensity of the visible contribution of the crystalline Si substrate (c-Si) depends on the thickness and transparency of the chalcogenide films at 532 nm.

In Fig. 2c, the FTIR and Raman spectra of the $[Ge_{40}S_{60}]_{1-x}[Ge_{26}Se_{74}]_x$ thin films obtained by co-sputtering of $Ge_{40}S_{60}$ and $Ge_{26}Se_{74}$ targets exhibit the main modes related to Ge–S and Ge–Se bonds with broadening and a slight frequency shift of their intensity maxima compared with those detected in pure amorphous $Ge_{40}S_{60}$ and $Ge_{26}Se_{74}$ compounds[31]. The relative intensities of these two main contributions depend on the $Ge_{40}S_{60}/Ge_{26}Se_{74}$ concentration ratio introduced in the film during co-sputtering. Besides, random incorporation of sulphur and selenium in mixed $GeS_{4-m}Se_m$ tetrahedra (with m = 1, 2 and 3) is observed as supported by previous experimental and simulation studies[32–35].

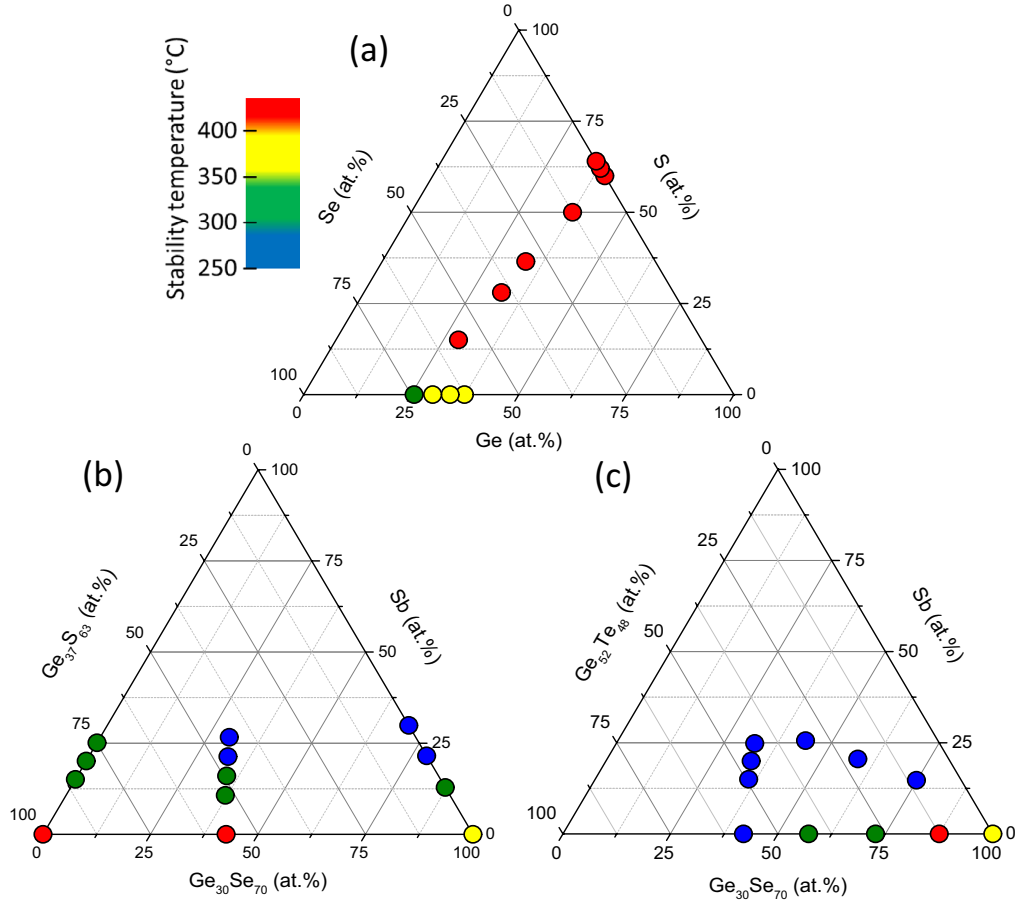

Figure 1. Ternary and pseudo-ternary diagrams showing compositions of the chalcogenide thin films deposited by magnetron (co)-sputtering: (**a**) $Ge_{1-x-y}S_xSe_y$, (**b**) $[Ge_{37}S_{63}]_{1-x-y}[Ge_{30}Se_{70}]_xSb_y$ and (**c**) $[Ge_{30}Se_{70}]_{1-x-y}[Ge_{52}Te_{48}]_xSb_y$ films. The dots' size denotes the error bars estimated on the compositions of the films and the dots' colour corresponds to an estimation of their limit temperature of stability defined by means of the temperature-resolved reflectivity measurements (see "Methods" and the Supplementary Information). Compounds' compositions indicated in square bracket correspond to those of the sputtering targets which may differ from those obtained for the deposited films.

$[Ge_{30}Se_{70}]_{1-x}Sb_x$, $[Ge_{37}S_{63}]_{1-x}Sb_x$ and $[Ge_{37}S_{63}]_{1-x-y}[Ge_{30}Se_{70}]_xSb_y$ thin films. Figure 3a shows the Raman and FTIR spectra acquired on the $[Ge_{30}Se_{70}]_{1-x}Sb_x$ films. Addition of Sb in $Ge_{30}Se_{70}$ films results in formation of $SbSe_{3/2}$ pyramids, which are reminiscent of the main structural units of amorphous Sb_2Se_3, connected to $GeSe_{4/2}$ tetrahedral units by the Se atoms, and a decreasing number of Se–Se homopolar bonds in favour of a more and more prominent amount of homopolar Sb–Sb and wrong Ge–Sb bonds. This observation is of a major importance since homopolar Sb–Sb and wrong Ge–Sb bonds are shown to play a major role on electronic and hence optical properties of chalcogenide glasses[3,36,37]. Apart the non-negligible amount of Sb–Sb and Ge–Sb bonds present in our films which are chalcogen-deficient compared with the $GeSe_2$ and Sb_2Se_3 stoichiometric compositions, a similar trend has been previously observed in $[GeSe_2]_{1-x}[Sb_2Se_3]_x$ bulk glasses[38].

The FTIR and Raman spectra of the $[Ge_{37}S_{63}]_{1-x}Sb_x$ thin films are shown in Fig. 3b. S-deficient $[Ge_{37}S_{63}]_{1-x}Sb_x$ films are mainly composed of $GeS_{4/2}$ tetrahedral units and, upon addition of pure Sb, Sb–Sb and Sb–Ge bonds are formed with appearance of a small amount of $SbS_{3/2}$ pyramids. Therefore, in other words the amorphous network of our S-poor glasses can be depicted as a mix of $GeSb_{4-m}S_m$ tetrahedral motifs (with $m = \{0, 1, 2, 3, 4\}$) and few $SbGe_{3-m-n}Sb_mS_n$ pyramidal units (with $n + m = \{0, 1, 2, 3\}$) in favour of homopolar Sb–Sb and wrong Sb–Ge bonds[39–42].

In Fig. 3c, the FTIR and Raman spectra of the $[Ge_{37}S_{63}]_{1-x}[Ge_{30}Se_{70}]_x$ thin films upon Sb incorporation show vanishing of the Raman modes of mixed $GeS_{4-m}Se_m$ tetrahedral units at least in favour of an increase number of $GeSe_{4/2}$ tetrahedra. This indicates differences between Ge and Sb atoms in chemical bonding affinity with S and Se chalcogen elements. This has a different impact on the amorphous structure depending on the S/Se ratio. Increasing Sb concentration in $[Ge_{37}S_{63}]_{1-x-y}[Ge_{30}Se_{70}]_xSb_y$ films leads to preferential formation of Ge–Se and Sb–S bonds by detriment to Ge–S and Sb–Se ones in films exhibiting a lack of chalcogen element compared with the stoichiometric compositions in agreement with a previous study[41]. Raman and in a less manner FTIR

System	Bond	Main structural motifs	Raman modes (cm^{-1})	References	IR modes (cm^{-1})	References
$Ge_{1-x}Se_x$	Ge–Se	$GeSe_{4/2}$ tetrahedra	115; 140	68,69	115; 260; 285; 310	69
		CS $GeSe_{4/2}$ tetrahedra	195	70	–	–
		ES $GeSe_{4/2}$ tetrahedra	218; 310	70	–	–
		ETH Ge_2Se_6 units	–	–	220	69
	Ge–Ge	ETH Ge_2Se_6 units	179; 270	24,70	–	–
		Ge tetrahedra in amorphous Ge phase	275	71	–	–
	Se–Se	Se–Se bridge between $GeSe_{4/2}$ tetrahedra	265	14	–	–
$Ge_{1-x}S_x$	Ge–S	$GeS_{4/2}$ tetrahedra	115; 150	72,73,74	147; 367; 388	75,76
		CS $GeS_{4/2}$ tetrahedra	343; 425	70,72,76	343	75
		ES $GeS_{4/2}$ tetrahedra	370; 437	70,72,76	437	75
	Ge–S–Ge	$GeS_{4/2}$ tetrahedra	–	–	265	32
	Ge–Ge	ETH Ge_2S_6 units	250	30,70	–	–
	S–S	S rings	220; 475	73	–	–
		S chains	485	32	–	–
$Ge_{1-x-y}S_xSe_y$	Ge–Se	GeS_1Se_3 mixed tetrahedra	218	34,35	–	–
		GeS_2Se_2 mixed tetrahedra	232	34,35	–	–
		GeS_3Se_1 mixed tetrahedra	265	35	–	–
	Ge–S	GeS_1Se_3 mixed tetrahedra	392	35	–	–
		GeS_2Se_2 mixed tetrahedra	383	35	–	–
		GeS_3Se_1 mixed tetrahedra	367	35	–	–
$Ge_{1-x-y}Sb_xSe_y$	Sb–Se	$SbSe_{3/2}$ pyramids	190	14	180; 200; 250	32,77
	Sb–Sb	ETH Sb_2Se_4 units	159	14	156	78
		amorphous Sb phase	140	79,80	–	–
	Ge–Sb	amorphous $Ge_{15}Sb_{85}$ phase	140	81	–	–
$Ge_{1-x-y}Sb_xS_y$	Sb–S	$SbS_{3/2}$ pyramids	280; 308	82	285; 330	83,84
	Sb–Sb	ETH Sb_2S_4 units	170	40	–	–
	Ge–Sb	$S_3Ge–SbS_2$ units	205	85	–	–
$Ge_{1-x-y}Se_xTe_y$	Ge–Te	$GeTe_{4/2}$ tetrahedra		–	150; 220	86
	Ge–Te	Ge–$GeTe_3$ tetrahedra or GeTe defective octahedral motifs	120	87	–	–
	Se–Te	Se–Te–Se bridge between $GeSe_{4/2}$ tetrahedra	200	22,88	–	–
	Te–Te	Te chains	150	89	–	–
		amorphous Te phase	157	90,91	–	–
$Ge_{1-x-y-z}Sb_xSe_yTe_z$	Sb–Te	$SbTe_{3/2}$ pyramids	145	92	–	–
Si substrate	Si–Si	c–Si modes	300; 520	93	–	–

Table 1. List of bonds and their main vibration frequencies in the corresponding structural motifs as detected by Raman and FTIR analysis of chalcogenide thin films. The frequencies of the Raman and FTIR modes correspond to position of experimental peaks reported for stoichiometric glasses in the literature. The analysis of these peaks is extensively discussed in Sect. 3 of the Supplementary Information. CS, ES and ETH denotes respectively corner-sharing, edge-sharing and ethane-like motifs as commonly labelled in the literature.

spectra also evidences the presence of a significant amount of Ge–Ge, Sb–Sb and Ge–Sb bonds in our sputtered $[Ge_{37}S_{63}]_{1-x-y}[Ge_{30}Se_{70}]_xSb_y$ films.

$[Ge_{30}Se_{70}]_{1-x}[Ge_{52}Te_{48}]_x$, $[Ge_{30}Se_{70}]_{1-x-y}[Ge_{52}Te_{48}]_xSb_y$ and $[Ge_{1-2x}Se_xTe_x]_{1-y}Sb_y$ thin films. Figure 4a shows the FTIR and Raman spectra acquired on the $[Ge_{30}Se_{70}]_{1-x}[Ge_{52}Te_{48}]_x$ thin films obtained by co-sputtering of $Ge_{30}Se_{70}$ and $Ge_{52}Te_{48}$ targets. Ge-$GeTe_3$ tetrahedra and GeTe defective octahedral motifs present in a-GeTe phase[43,44] are expected also in $Ge_{52}Te_{48}$-rich $[Ge_{30}Se_{70}]_{1-x}[Ge_{52}Te_{48}]_x$ films. The structure of our $[Ge_{30}Se_{70}]_{1-x}[Ge_{52}Te_{48}]_x$ thin films obtained by co-sputtering can be depicted as $GeSe_{4-n}Te_n$ tetrahedral motifs with n = {0, 1, 2, 3, 4} forming a disordered network connected, for small x values, by means of the chalcogen elements and, for higher x values, coexisting with a non-negligible amount of Ge–Ge homopolar bonds and possibly some Te–Te bonds as well as Se–Te bonds as proposed in a previous work[22].

In Fig. 4b,c are shown the FTIR and Raman spectra of $[Ge_{30}Se_{70}]_{1-x-y}[Ge_{52}Te_{48}]_xSb_y$ and $[Ge_{1-2x}Se_xTe_x]_{1-y}Sb_y$ thin films obtained by co-sputtering of $Ge_{30}Se_{70}$, $Ge_{52}Te_{48}$ and Sb targets. The comparison between both figure tends to indicate that in our amorphous $[Ge_{30}Se_{70}]_{1-x}[Ge_{52}Te_{48}]_x$ films, which are getting more and more Ge-rich as x value is increased, Ge–Ge homopolars are found and Ge–Se(Te) bonds represent the vast majority of

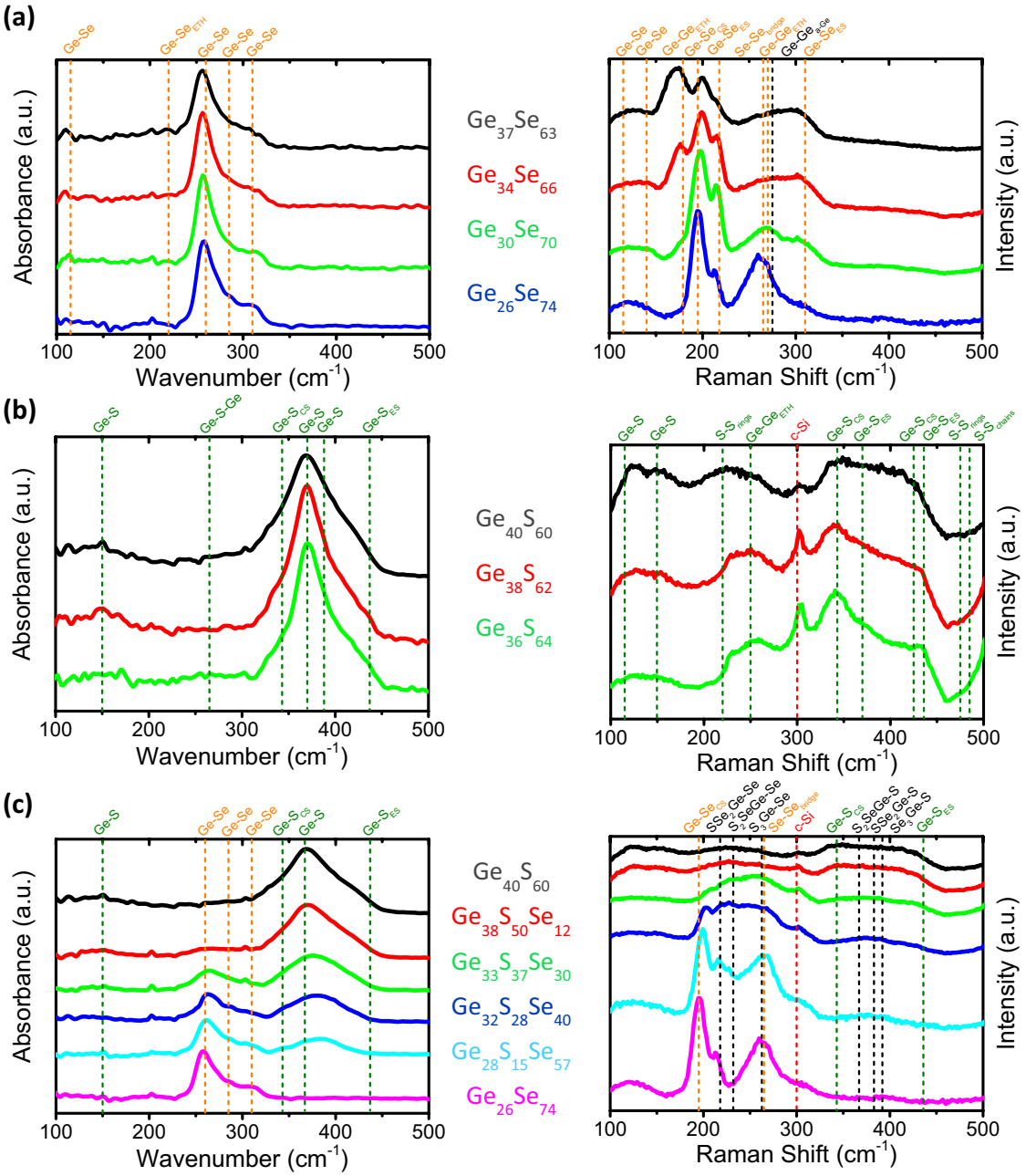

Figure 2. FTIR and Raman spectra of as-deposited (**a**) $Ge_{1-x}Se_x$ (**b**) $Ge_{1-x}S_x$ and (**c**) $[Ge_{40}S_{60}]_{1-x}[Ge_{26}Se_{74}]_x$ thin films. The different contribution of vibration modes related to $GeSe_2$ and GeS_2 amorphous phases are indicated by orange and green dash-lines, respectively. The contribution of the c-Si substrate to the Raman signal appearing on some spectra is also indicated by a red dash-line at 300 cm^{-1} as well as a shoulder visible after 450 cm^{-1} that corresponds to a c-Si phonon mode near 520 cm^{-1}.

bonds involving the chalcogen elements. Upon introduction of Sb in the $[Ge_{30}Se_{70}]_{1-x}[Ge_{52}Te_{48}]_x$ films, whereas the contribution of Sb–Se bonds to the Raman spectra is weak their presence in IR absorption is more visible in FTIR spectra probably thanks to the high IR cross section of such bonds compared with others. Sb doping of the $Ge_{43}Se_{29}Te_{28}$ compound lead to formation of Sb-Sb homopolar bonds and probably Ge–Sb wrong bonds as already discussed above for Sb-doped $Ge_{30}Se_{70}$ films. As a result, $[Ge_{30}Se_{70}]_{1-x-y}[Ge_{52}Te_{48}]_xSb_y$ films obtained by co-sputtering appear to be a highly disordered system. It can be depicted as a mix of Ge–$GeTe_3$ and $GeSb_{4-m-n}Se_mTe_n$ tetrahedra (with $m+n=\{0, 1, 2, 3, 4\}$) as well as $SbGe_{3-m-n}Se_mTe_n$ motifs (with $m+n=\{0, 1, 2, 3\}$). The relative fraction between these motifs varies as a function of the Ge/Se/Te atomic ratio of the films.

To conclude, the effect of Sb incorporation in the amorphous structure of $[Ge_{37}S_{63}]_{1-x}[Ge_{30}Se_{70}]_x$ and $[Ge_{30}Se_{70}]_{1-x}[Ge_{52}Te_{48}]_x$ thin films is different depending on the nature of the chalcogen elements present in the film. A clear difference is observed between films containing S/Se compared with Se/Te as chalcogen elements. In particular, this is evidenced by formation of $GeSb_{4-m-n}Se_mTe_n$ tetrahedra (with $m+n=\{0, 1, 2, 3, 4\}$) as well

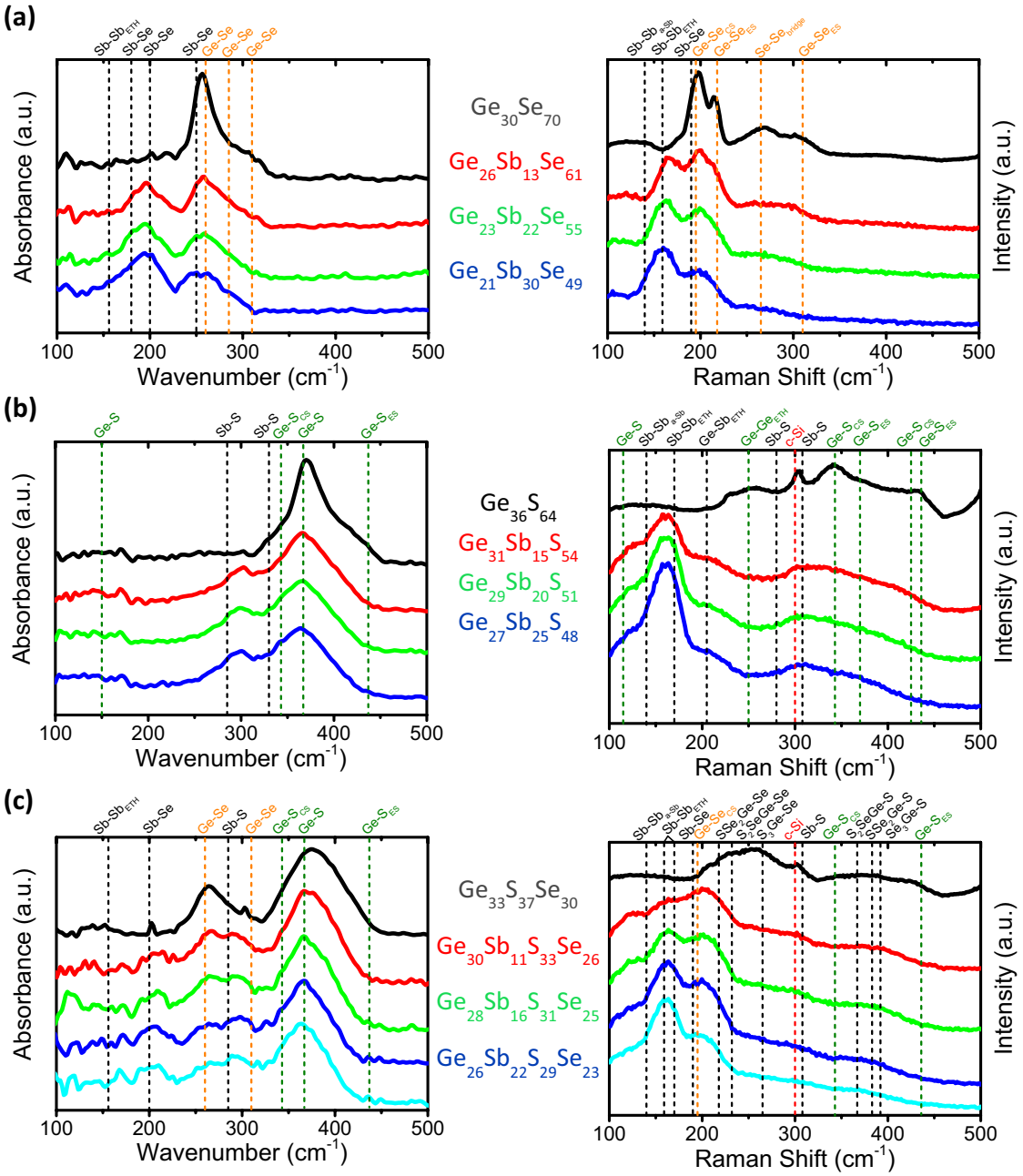

Figure 3. FTIR and Raman spectra of (**a**) $[Ge_{30}Se_{70}]_{1-x}Sb_x$ (**b**) $[Ge_{37}S_{63}]_{1-x}Sb_x$ and (**c**) $[Ge_{37}S_{63}]_{1-x-y}[Ge_{30}Se_{70}]_xSb_y$ thin films. The position of the main vibration modes related to $GeSe_2$ and GeS_2 stoichiometric glasses are indicated by orange and green dash-lines, respectively. The contribution of the c-Si substrate to the Raman signal appearing on some spectra is also indicated by a red dash-line at 300 cm^{-1} as well as a shoulder visible after 450 cm^{-1} that corresponds to a c-Si phonon mode near 520 cm^{-1}.

as $SbGe_{3-m-n}Se_mTe_n$ motifs (with $m+n=\{0, 1, 2, 3\}$) in Sb-doped $[Ge_{30}Se_{70}]_{1-x}[Ge_{52}Te_{48}]_x$ thin films whereas no such mixed Ge tetrahedra nor mixed Sb pyramids can be observed in $[Ge_{37}S_{63}]_{1-x}[Ge_{30}Se_{70}]_x$ compounds doped with Sb. Besides, in both case Sb addition $[Ge_{37}S_{63}]_{1-x}[Ge_{30}Se_{70}]_x$ and $[Ge_{30}Se_{70}]_{1-x}[Ge_{52}Te_{48}]_x$ films does not lead to a random and homogeneous distribution of the chalcogen atoms in Ge-centered tetrahedra as observed in Ge-based chalcogenide films. From all the above FTIR and Raman study, one can conclude that the local order and the structure of the (co-)sputtered chalcogenide thin films are shown to largely vary with in particular a very different amount of homopolar bonds and the latter is shown to depend on thin films' atomic composition. Since the properties of materials being intimely linked to their structure, probing the link between structure and optical properties is an invaluable clue in order to propose design rules aiming at fabricating chalcogenide compounds thin films with optimized properties for the applications in photonics. In the following, the linear and nonlinear optical constants of the films, such as the real and imaginary part of refractive index as well as Kerr nonlinear refractive index, are studied.

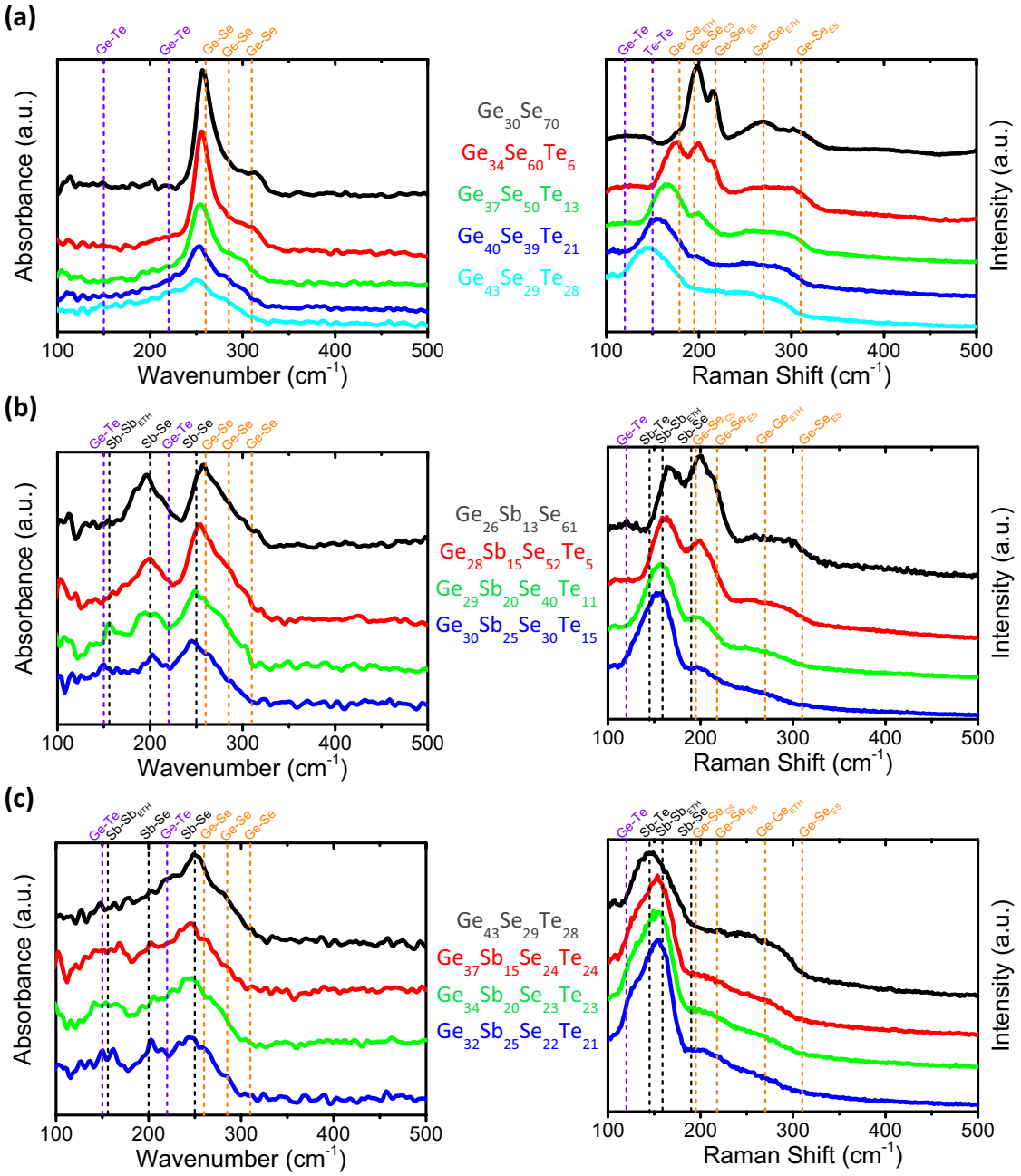

Figure 4. FTIR and Raman spectra of (**a**) $[Ge_{30}Se_{70}]_{1-x}[Ge_{52}Te_{48}]_x$, (**b**) $[Ge_{30}Se_{70}]_{1-x-y}[Ge_{52}Te_{48}]_xSb_y$ and (**c**) $[Ge_{1-2x}Se_xTe_x]_{1-y}Sb_y$ thin films. The position of the main modes related to amorphous GeTe or $GeSe_2$ compounds as well as those related to Sb atoms are indicated by orange, purple and black dash-lines, respectively.

Optical properties of the chalcogenide thin films. *Linear optical constants.* The optical constants (refractive index n and extinction coefficient k) of the films were deduced from the spectroscopic ellipsometry measurements from visible to near-IR (NIR) range (see "Methods"). The refractive indices n and Tauc's plots of $(\alpha.E)^{1/2}$ vs energy (eV) obtained from the extinction coefficient k (see "Methods") are plotted in Figs. 5, 6, 7 for each composition of the chalcogenide films. First, Figs. 5, 6, 7 call for a general comment. For wavelength range located above inter band absorption range, which corresponds to energies lower than the bandgap energy (see the Tauc's plots of Figs. 5, 6, 7), the refractive indices tend progressively to a kind of plateau. The latter gives therefore an estimation of the refractive indices in the MIR range up to multi-phonons absorption appearing at significantly higher wavelengths than NIR[45,46]. Therefore, the study of optical properties in the visible-NIR range is the best compromise in order to get an estimation of refractive indices from visible to MIR range as well as giving an estimation of the optical band gap energy from absorption measurements or ellipsometry data fitting models (see "Methods" and Sect. 4 of the Supplementary Information).

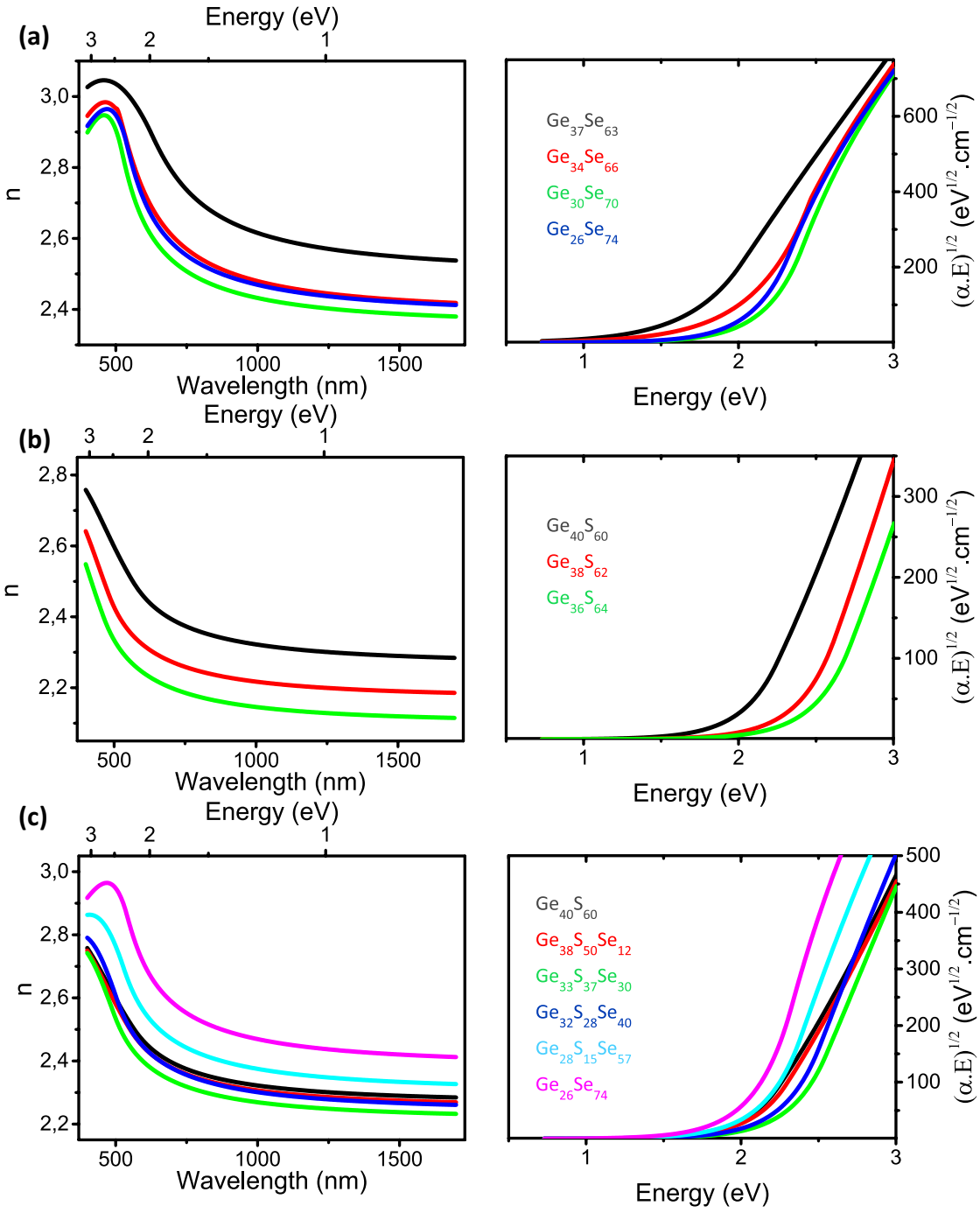

Figure 5. Refractive index n (left panels) and Tauc's plots (right panels) of (**a**) $Ge_{1-x}Se_x$ (**b**) $Ge_{1-x}S_x$ and (**c**) $[Ge_{40}S_{60}]_{1-x}[Ge_{26}Se_{74}]_x$ thin films deposited by (co-)sputtering.

$Ge_{1-x}Se_x$, $Ge_{1-x}S_x$ and $[Ge_{40}S_{60}]_{1-x}[Ge_{26}Se_{74}]_x$ thin films. In Fig. 5a, the refractive index of the sputtered $Ge_{1-x}Se_x$ ($0.63 < x < 0.74$) thin films in the NIR range (above 850 nm) does not evolve linearly with composition but reaches a maximum for $x = 0.63$ as well as a minimum for $x = 0.7$. This effect can be related to the amorphous structure of $Ge_{37}Se_{63}$ film which exhibits the highest amount of Ge–Ge homopolar bonds in ethane-like structures among all $Ge_{1-x}Se_x$ ($0.63 < x < 0.74$) films (see the Raman of Fig. 2a). Besides, ab initio molecular dynamics simulations reported that the presence of numerous distorted Se–Ge–Se angles in $Ge_{1-x}Se_x$ ($0.60 < x < 0.66$) permits to reduce the stress induced by the increase of the Ge content and thus the mean atomic coordination number or network connectivity[47]. By opposite, the $Ge_{30}Se_{70}$ film which has the lowest refractive index also presents the lowest amount of Ge–Ge and Se–Se homopolars and the narrowest and most well-defined modes corresponding to CS and ES $GeSe_{4/2}$ tetrahedra (195 and 212 cm^{-1}) as shown in Fig. 2a. This trend on the refractive index is in good agreement with previous literature for bulk glasses in which compositions with the highest Ge–Se/(Ge–Ge + Se–Se) bonding ratio exhibited the lowest refractive indices[26]. The absorption of $Ge_{30}Se_{70}$

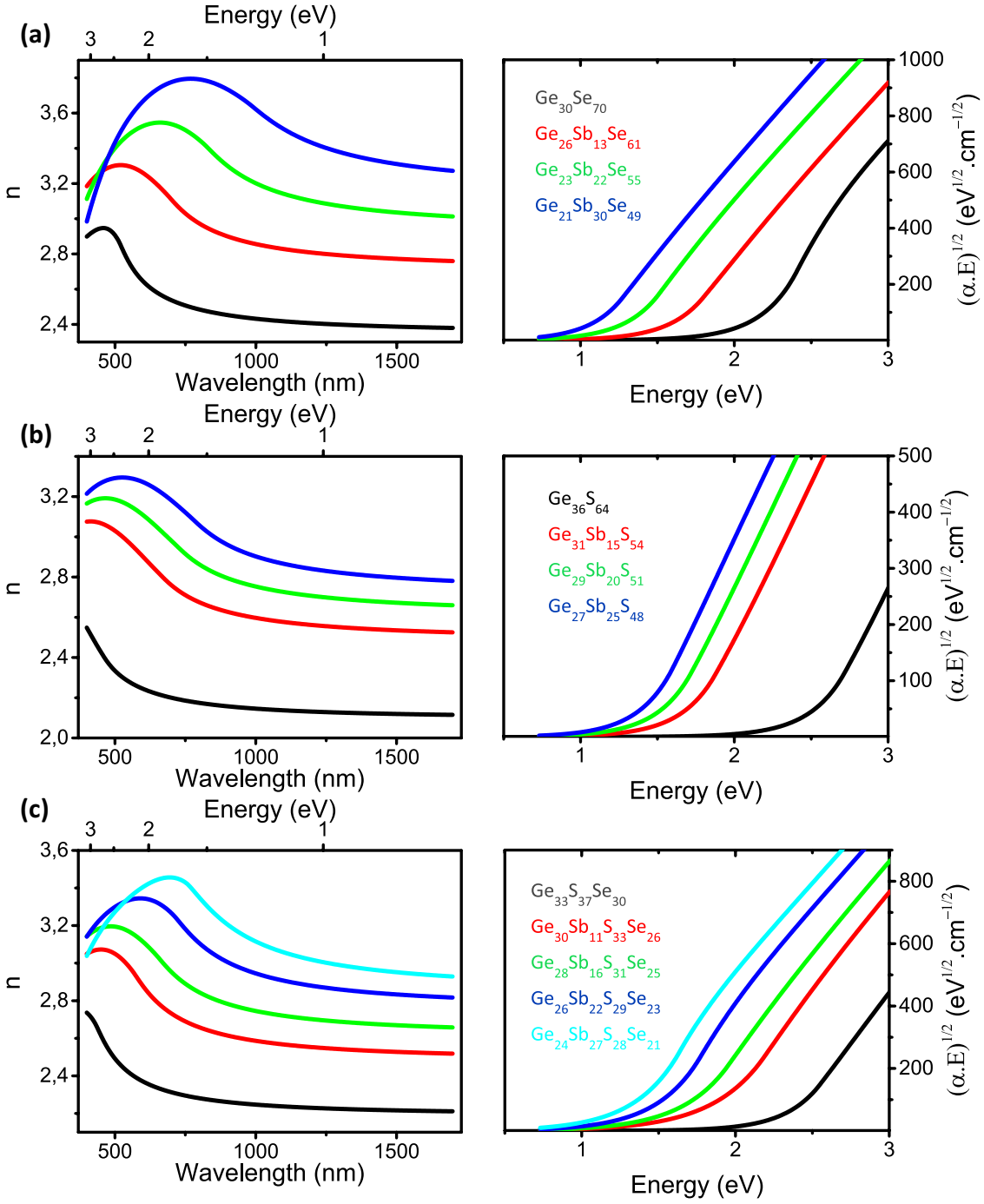

Figure 6. Refractive index n and Tauc's plots of (**a**) $[Ge_{30}Se_{70}]_{1-x}Sb_x$ (**b**) $[Ge_{37}S_{63}]_{1-x}Sb_x$ and (**c**) $[Ge_{37}S_{63}]_{1-x-y}[Ge_{30}Se_{70}]_xSb_y$ thin films deposited by (co-)sputtering.

film evidences its highest band gap value among all $Ge_{1-x}Se_x$ ($0.63 < x < 0.74$) films as seen on the Tauc's plots of Fig. 5a. Besides, the $Ge_{37}Se_{63}$ composition with the highest refractive index has the lowest band gap energy. The decreasing number of Ge–Ge bonds may be at origin of the strong increase of absorption between $Ge_{34}Se_{66}$ and $Ge_{37}Se_{63}$ films.

$Ge_{1-x}S_x$ thin films experience a significant increase of their refractive index in the NIR as the Ge fraction is slightly increased from $x = 0.64$ to $x = 0.60$ (Fig. 5b). This trend is consistent with previous literature studies[48,49]. This could be attributed to an increasing number of distorted S–Ge–S bonds similarly to the previously mentioned presence of numerous distorted Se–Ge–Se angles in $Ge_{1-x}Se_x$ ($0.60 < x < 0.66$)[47] related to the increase of the number of Ge–Ge homopolar bonds (see Fig. 2b) with the decrease of the S content. This leads to a reduction of the band gap energy in agreement with previous literature[49] due to creation of new electronic states under the conduction band explaining the progressive shift of absorption toward lower energy (Fig. 5b)[50]. The absorption and refractive index change monotonously as x increases in our $Ge_{1-x}S_x$ films (Fig. 5b).

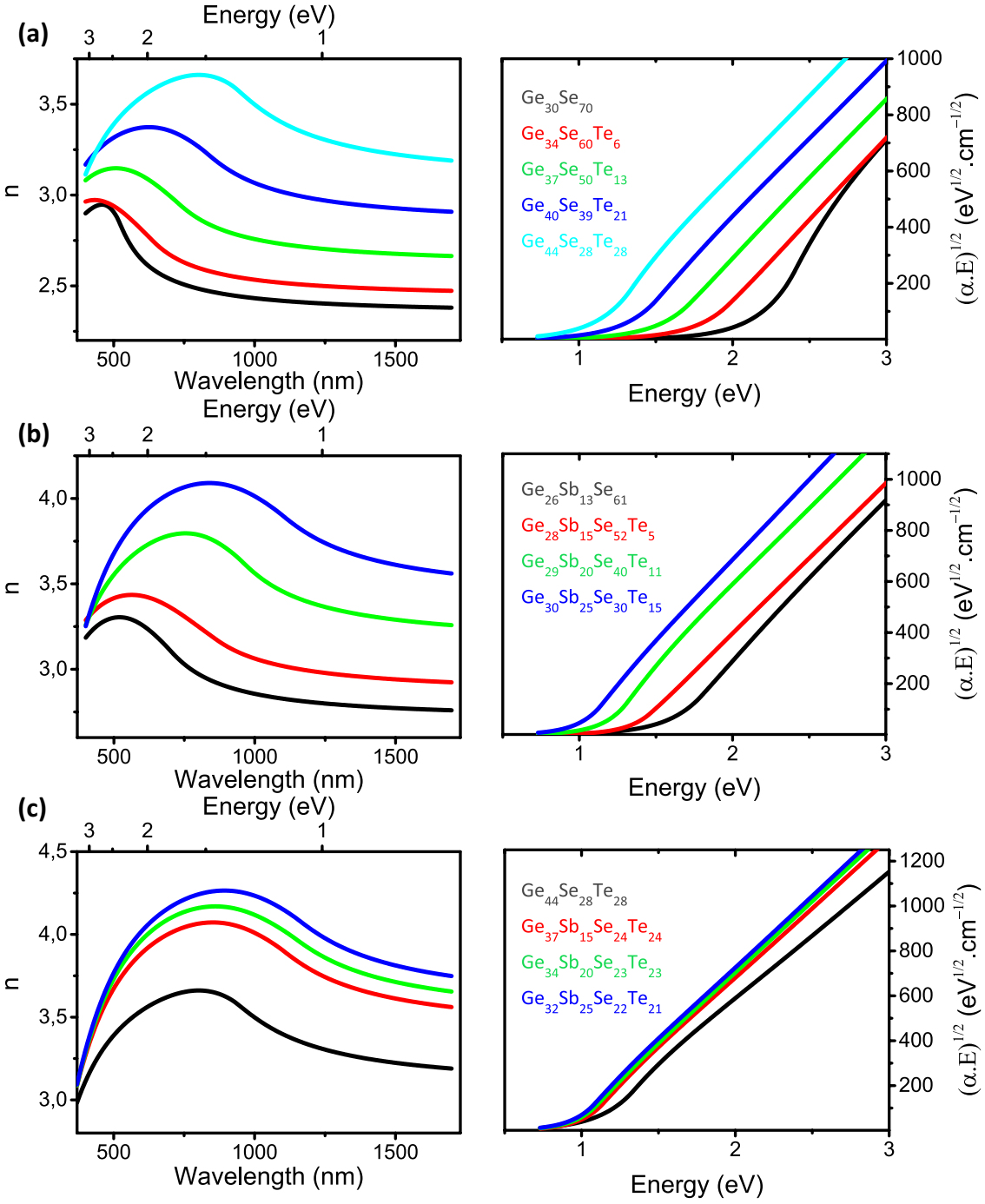

Figure 7. Refractive index n and Tauc's plots of (**a**) $[Ge_{30}Se_{70}]_{1-x}[Ge_{52}Te_{48}]_x$ (**b**) $[Ge_{30}Se_{70}]_{1-x-y}[Ge_{52}Te_{48}]_xSb_y$ and (**c**) $[Ge_{1-2x}Se_xTe_x]_{1-y}Sb_y$ thin films deposited by (co-)sputtering.

The refractive index of the $[Ge_{40}S_{60}]_{1-x}[Ge_{26}Se_{74}]_x$ films also exhibits a minimum for the $Ge_{33}S_{37}Se_{30}$ composition (Fig. 5c). This is not surprising since, similarly to $Ge_{1-x}Se_x$ and $Ge_{1-x}S_x$ films, the amount of Ge–Ge homopolar bonds is expected to be minimum for this near-stoichiometric composition with a Ge/(S + Se) atomic ratio close to 1/2 (Fig. 2c). As a result, the general trends on refractive indices of studied Ge-based chalcogenide films are driven by the ratio between heteropolar and homopolar bonds.

Among the $[Ge_{40}S_{60}]_{1-x}[Ge_{26}Se_{74}]_x$ thin films, the band gap energy reaches a maximum for the $Ge_{33}S_{37}Se_{30}$ composition as evidenced by the absorption curves in Fig. 5c. This results from the composition of $Ge_{33}S_{37}Se_{30}$ film which is close to the $GeCh_2$ stoichiometric compound (with Ch referring to S or Se chalcogen element) expected to exhibit almost no homopolar bonds. Note that for a same Ge concentration, replacing S by Se atoms results in a progressive decrease of band gap energy[31].

$[Ge_{30}Se_{70}]_{1-x}Sb_x$, $[Ge_{37}S_{63}]_{1-x}Sb_x$ and $[Ge_{37}S_{63}]_{1-x-y}[Ge_{30}Se_{70}]_xSb_y$ thin films. In Fig. 6, replacing tetravalent Ge atoms, as observed in structural motifs of stoichiometric $GeSe_2$ glass, by trivalent Sb atoms, as found in amorphous stoichiometric Sb_2Se_3 compound, within the GeS_xSe_{1-x} films increases the non-chalcogen/chalcogen element ratio required to keep the stoichiometric composition. This has been clearly evidenced for composition tie-lines crossing the stoichiometric $GeSe_2/Sb_2Se_3$ pseudo-binary tie-line as $Ge_{40-x}Sb_xSe_{60}$[51], $Ge_xSb_{10}Se_{90-x}$[52,53] $Ge_xSb_{15}Se_{85-x}$ or $Ge_xSb_{20}Se_{80-x}$[53] glasses. These compositions are again those with the smallest amount of homopolar bonds and corresponding to a limit of topological phase transition as reported in $Ge_{40-x}Sb_xSe_{60}$ glasses[54,55]. Besides, in bulk glasses as well as in thin films, the decrease of the $GeSe_2/Sb_2Se_3$ ratio was shown to result in an increase of the refractive index and a decrease of the band gap energy since electronic polarizability of Sb–Se bonds is much higher than that of Ge-Se bonds[24,56,57].

In Fig. 6 are shown the change of optical constants upon Sb addition by means of co-sputtering in the $Ge_{30}Se_{70}$, $Ge_{33}S_{67}$ and $[Ge_{33}S_{67}]_{1-x}[Ge_{30}Se_{70}]_x$ thin films in order to increase films' refractive indices by drifting away from compositions located on the $GeCh_2/Sb_2Ch_3$ pseudo-binary tie-line. In Figs. 6a–c the incorporation of Sb in $Ge_{30}Se_{70}$, $Ge_{33}S_{67}$ and $[Ge_{33}S_{67}]_{1-x}[Ge_{30}Se_{70}]_x$ films significantly increases films' refractive index and at the same time reducing the optical band gap energy of the material. This effect is attributed to the higher electronic polarizability of Sb atoms in particular when forming Sb–Ch and Sb–Sb bonds. These highly polarizable bonds are revealed to appear in an increasing level as the incorporated Sb amount is increased in films (see amorphous structure analysis detailed in the Amorphous Structure section and in the Supplementary Information). One can also note that among all these compositions, some films exhibit compositions very close to those of well-studied commercial glasses such as for instance AMTIR-3 glass (also commercially called IG5 or IRG-5 or BD-2 or OPTIR-3) of $Ge_{28}Sb_{12}Se_{60}$ composition. Thus, this well-known glass is close to the $Ge_{26}Sb_{13}Se_{61}$ film of the present study and can be used as a point of comparison. In Fig. 6a, the optical constant values of our $[Ge_{30}Se_{70}]_{1-x}Sb_x$ films are in good agreement with the literature[14,52,53].

$[Ge_{30}Se_{70}]_{1-x}[Ge_{52}Te_{48}]_x$, $[Ge_{30}Se_{70}]_{1-x-y}[Ge_{52}Te_{48}]_xSb_y$ and $[Ge_{1-2x}Se_xTe_x]_{1-y}Sb_y$ thin films. Figure 7a shows that, similarly to Sb, introduction of $Ge_{52}Te_{48}$ in $[Ge_{30}Se_{70}]_{1-x}[Ge_{52}Te_{48}]_x$ films results in a huge increase of refractive index of the $Ge_{30}Se_{70}$ glass. As in the Sb doping, this effect could be attributed to the higher electronic polarizability of atoms of Ge–Te motifs compared with those in Ge-Se ones, and that form in a growing concentration in $[Ge_{30}Se_{70}]_{1-x}[Ge_{52}Te_{48}]_x$ films upon increasing the $Ge_{52}Te_{48}$ concentration (see Fig. 4a). Moreover, the refractive index of $[Ge_{30}Se_{70}]_{1-x}[Ge_{52}Te_{48}]_x$ films can be further increased by Sb incorporation as shown in Fig. 7b,c. Such an increase is near directly correlated to the concentration of Te and Sb atoms in the $[Ge_{30}Se_{70}]_{1-x-y}[Ge_{52}Te_{48}]_xSb_y$ and $[Ge_{1-2x}Se_xTe_x]_{1-y}Sb_y$ films with a more and more significant effect when highly polarizable environments such as Sb–Te, Sb-Sb bonds or in a less extent Ge–Te bonds form in the amorphous material[58].

In Fig. 7a, the increase of absorption of $[Ge_{30}Se_{70}]_{1-x}[Ge_{52}Te_{48}]_x$ films upon increasing x can be related to the smallest bandgap of a-GeTe compared to that of Se-based compound[59]. The absorption progressively decreases as the band gap of the film increases upon moving toward the $Ge_{30}Se_{70}$ composition. By opposite, in Fig. 7b,c for $[Ge_{30}Se_{70}]_{1-x-y}[Ge_{52}Te_{48}]_xSb_y$ films, a more complex trend is observed. First, in Fig. 7b an increase of the (Sb + Te)/Se ratio in $[Ge_{30}Se_{70}]_{1-x-y}[Ge_{52}Te_{48}]_xSb_y$ films lead to a shift of the absorption curve toward lower energy due to a decrease of band gap energy. More surprising, in Fig. 7c the absorption curves and optical band gap of $[Ge_{1-2x}Se_xTe_x]_{1-y}Sb_y$ films remain almost constant for the three compounds containing Sb concentration ranging from 15 to 30 at. %. Increasing the concentration of homopolar bonds, mainly Sb-Sb ones, and Te-related bonds due to an increase of the (Sb + Te)/Se ratio in $[Ge_{30}Se_{70}]_{1-x-y}[Ge_{52}Te_{48}]_xSb_y$ films result in an increase of band tails as well as creation of electronic states in the bandgap, and hence to a reduction of the optical bandgap energy.

However, in Fig. 7c upon incorporation of Sb in the ternary $Ge_{1-2x}Se_xTe_x$ compound, the refractive index of the films significantly increase while the decrease in bandgap energy is negligible. The explanation is related to the changes in the amorphous structure. First, the increasing concentration of Sb leads to an increase of the material polarizability and thus that of the refractive index. However, at the same time the amount of Te–Ge heteropolar bonds decreases leading to an increase of band gap energy of the material hence counterbalancing the effect of Sb. Therefore in $[Ge_{1-2x}Se_xTe_x]_{1-y}Sb_y$ films, the incorporation of highly polarizable Sb bonds leads to an increase of the refractive index but does not significantly affect the optical band gap energy value. Indeed, the replacement of Ge–Ge homopolars by Sb–Sb bonds upon Sb introduction is expected to impact mostly the density and nature of localized electronic defect states in the material band gap but with no or limited effect on the bandgap energy.

To summarize, the observed trend of refractive indices as a function of chalcogenide thin films' compositions can be reasonably correlated to changes in films' amorphous structure as extensively described in the FTIR/Raman experiments of the Amorphous Structure section and in Sect. 3 of the Supplementary Information. The electronic polarizability of local chemical environments and bonding configurations in the amorphous is shown to play key role aiming at controlling the refractive indices of the films. In particular, introduction of highly polarizable bonds such as Sb–Sb homopolars, Sb–Ch (with Ch = Te or Se) or Te-X (with X = Sb or Ge) and in a less extent Ge–Ge bonds leads to a significant increase of the refractive index concomitant to a decrease of the optical bandgap energy. The optical band gap energy is also an outmost parameter that should be taken into account for MIR and nonlinear photonic applications regarding for instance transparency window, two-photon absorption (TPA) losses and so on. The band gap energy values of the chalcogenide thin films are listed in Table 2. The obtained band gap energies and refractive index values are found to follow the well-known Moss rule[60], which relates the refractive index (or optical dielectric constant) to the optical band gap energy of semiconductors[61].

In order to evaluate the potential interest for applications of such chalcogenide thin films in the emerging field of on-chip nonlinear photonics, determining the Kerr refractive indices, which quantify the nonlinear frequency conversion efficiencies, can give a first interesting insight. For that purpose, in the following the Kerr

refractive indices of the films are estimated by means of their linear optical constants as well as using estimated values of the band gap energy.

Kerr nonlinear refractive indices n_2. The n_2 Kerr nonlinear refractive indices were evaluated mainly using the Sheik–Bahae model[29]. We considered this model as enough accurate in order to get qualitative trends on n_2 values (see Sect. 5 of the Supplementary Information). It has to be emphasized that a systematic error of about 20% exists in the experimental determination of non-linear optical coefficients.

The Kerr refractive index is strongly correlated with the linear refractive index and the optical band gap energy value. Using the Sheik–Bahae model, the maximum of the third order nonlinear parameter is found for an energy close to $0{,}534 \times E_g^{opt}$. Therefore, the values of n_2 can vary considerably depending on the wavelength and must be taken into consideration depending on the value of the wavelength that will be used in the application. However, previous experimental work reported a maximum of Kerr index for photon energy values higher than that corresponding to $0{,}534 \times E_g^{opt}$ [53]. Table 2 shows the maximum values of the n_2 Kerr refractive indices for all the films studied in this work and their corresponding wavelengths, as well as the values obtained at 1,550 nm, the standard wavelength for telecommunications. In order to validate the Sheik–Bahae model, this method was also applied to samples of silica and silicon nitride thin film. The n_2 values at 1,550 nm for these two reference materials have been calculated to be 3×10^{-20} and 2×10^{-19} m^2/W, respectively. These values are in excellent agreement with those experimentally measured in the literature[60]. Therefore, one can conclude that in our (co-)sputtered amorphous chalcogenide thin films, the Kerr indices are of two to three orders of magnitude higher than those obtained for silica or silicon nitride materials. These values are also in excellent agreement with previous experimental results reported for similar $Ge_{1-x-y}Sb_xSe_y$, $Ge_{1-x-y}Sb_xS_y$ compounds[38,63–65] as well as those deduced using the Sheik–Bahae model for $Ge_{1-x}S_x$ and $Ge_{1-x-y}Sb_xSe_y$ glasses[49,66].

For some of the chalcogenide thin films, the Sheik–Bahae model gives negative Kerr indices at 1,550 nm. In previous works, only positive experimental n_2 values were observed in the transparency window of chalcogenide glasses[61,67]. Nevertheless, negative Kerr indices values were reported in $Ge_{1-x-y}Sb_xSe_y$ glasses at 800 nm[66] where absorption starts to be non-negligible. Therefore, we can emphasize that the negative Kerr indices values at 1.55 μm (~ 0.8 eV) are found for co-sputtered films for which the optical band gap energy is below 1.6 eV and as a result when TPA becomes significant.

In literature, n_2 values have been related to the amorphous structure. In particular, a clear correlation was found between n_2 values and the concentration of highly polarizable heteropolar bonds[38]. Herein, one observe a clear correlation between material polarizability, which is proportional to the linear refractive index, and the nonlinearities evidenced by the n_2 values calculated by using the Sheik-Bahae model. Thus, one can relate the enhancement of electronic polarizability and the resulting increase of n_2 values to presence of peculiar local atomic motifs and bonding configurations found in the amorphous structure of films. For instance, the amount of homopolar bonds play a key role in the increase of linear and nonlinear refractive indices as described above.

Finally, in Table 2 are also reported for each films the limit of temperature after which a degradation of the material could be observed by monitoring optical reflectivity at 670 nm upon annealing (see "Methods" and Sect. 2 of the Supplementary Information). This is also very instructive since temperature limit in between 250 and 400 °C were obtained. This emphasizes that a compromise between optical properties and thermal stability has to be found for selection of a particular composition depending on final application as well as taking into account the thermal budget required for integration process flow in devices. Indeed, an annealing after deposition is also expected to significantly affect the optical properties of these Ge-based amorphous chalcogenide thin films due to the structural relaxation. Thus, aging of these metastable amorphous materials will have to be studied in the future aiming at ensuring durability of MIR components that would integrate some of these compounds.

Conclusion

To conclude, industrial co-sputtering deposition method is a powerful tool in order to fastly study a wide compositions range of amorphous chalcogenide thin films aiming at ultimately achieving highly nonlinear on-chip MIR components. By means of a systematic study of the amorphous structure correlated with the trend on optical properties (linear optical constants, optical band gap and Kerr nonlinear refractive index) of the as-deposited chalcogenide thin films one can get invaluable clues in order to optimize the materials optical properties towards future applications. The materials' polarizability and thus linear and nonlinear refractive indices increase significantly when moving from light to heavier chalcogen element such as S to Se and toward Te-based chalcogenide compounds but accompanied with a decrease of the thermal stability. The ratio of homopolar/wrong on heteropolar bonds in the amorphous chalcogenide is shown to play a main role on the electronic and thus optical properties of the films. For instance, the introduction of Sb atoms deeply modifies the amorphous structure as well as introducing Sb–Sb homopolar bonds. As a result, the electronic polarizability of the glass is significantly enhanced as evidenced by the significant increase of the material refractive indices. However, this also leads to a detrimental decrease of the material's thermal stability and bandgap. Moreover, we show that the outstanding and state-of-the-art Kerr refractive indices in the MIR range are found for chalcogenide thin films deposited by means of industrial sputtering technique enabling fast transfer to applications. Finally, we demonstrate that a good trade-off between high nonlinearity, good thermal stability and optimized working wavelength in the IR can be found opening wide range of opportunities for future on-chip photonic applications fully compatible with CMOS large-scale integration technologies.

Groups	Co-sputtered Targets			Compositions	E_g^{04} (eV)	E_g^{CL} (eV)	n λ = 1.55µm	n_2 (10^{-18} $m^2.W^{-1}$) λ = 1.55µm	$n_{2\,max}$ (10^{-18} $m^2.W^{-1}$)	Limit of thermal stability (°C)
$[Ge_{37}S_{63}]_{1-x}Sb_x$	$Ge_{37}S_{63}$		Sb	$Ge_{31}Sb_{15}S_{54}$	1.94	1.61	2.53	8.3	19.5 (λ = 1200 nm)	300
				$Ge_{29}Sb_{20}S_{51}$	1.76	1.46	2.67	13.6	25.9 (λ = 1320 nm)	300
				$Ge_{27}Sb_{25}S_{48}$	1.61	1.34	2.79	25.2	33.9 (λ = 1450 nm)	300
$Ge_{1-x}S_x$				$Ge_{36}S_{64}$	2.82	2.46	2.12	1.8	6.1 (λ = 820 nm)	400
				$Ge_{38}S_{62}$	2.7	2.37	2.19	2.1	6.8 (λ = 860 nm)	400
	$Ge_{40}S_{60}$			$Ge_{40}S_{60}$	2.39	1.98	2.29	3.4	10.2 (λ = 970 nm)	400
$Ge_{1-x-y}S_xSe_y$		$Ge_{25}Se_{75}$		$Ge_{38}S_{50}Se_{12}$	2.43	2.03	2.27	3.2	9.7 (λ = 960 nm)	400
				$Ge_{33}S_{37}Se_{30}$	2.57	2.3	2.24	2.5	8.0 (λ = 900 nm)	400
				$Ge_{32}S_{28}Se_{40}$	2.5	2.26	2.26	2.8	8.7 (λ = 930 nm)	400
				$Ge_{28}S_{15}Se_{57}$	2.35	2.15	2.33	3.6	10.5 (λ = 990 nm)	400
$Ge_{1-x}Se_x$				$Ge_{26}Se_{74}$	2.22	2.11	2.42	4.4	12.3 (λ = 1050 nm)	300
				$Ge_{30}Se_{70}$	2.29	2.19	2.39	3.8	11.1 (λ = 1010 nm)	350
			Ge	$Ge_{34}Se_{66}$	2.13	2.05	2.42	5.3	14.4 (λ = 1090 nm)	350
				$Ge_{37}Se_{63}$	1.88	1.64	2.55	9.9	21.8 (λ = 1240 nm)	350
$[Ge_{30}Se_{70}]_{1-x}[Ge_{52}Te_{48}]_x$	$Ge_{52}Te_{48}$	$Ge_{30}Se_{70}$		$Ge_{34}Se_{60}Te_6$	2.01	1.71	2.48	7.1	17.6 (λ = 1160 nm)	400
				$Ge_{37}Se_{50}Te_{13}$	1.73	1.46	2.67	15.2	27.7 (λ = 1350 nm)	300
				$Ge_{40}Se_{39}Te_{21}$	1.47	1.26	2.92	43.7	44.4 (λ = 1580 nm)	300
				$Ge_{44}Se_{28}Te_{28}$	1.23	1.12	3.21	19.4	75.7 (λ = 1890 nm)	250
$[Ge_{30}Se_{70}]_{1-x-y}[Ge_{52}Te_{48}]_xSb_y$			Sb	$Ge_{28}Sb_{15}Se_{52}Te_5$	1.54	1.29	2.94	35.6	36.6 (λ = 1510 nm)	250
				$Ge_{29}Sb_{20}Se_{40}Te_{11}$	1.3	1.14	3.28	30.1	58.6 (λ = 1790 nm)	250
				$Ge_{30}Sb_{25}Se_{30}Te_{15}$	1.13	0.97	3.6	-10.2	85.7 (λ = 2060 nm)	250
				$Ge_{37}Sb_{15}Se_{24}Te_{24}$	1.12	0.95	3.6	-13.7	88.7 (λ = 2080 nm)	250
				$Ge_{34}Sb_{20}Se_{23}Te_{23}$	1.09	0.93	3.69	-26.0	95.0 (λ = 2140 nm)	250
				$Ge_{32}Sb_{25}Se_{22}Te_{21}$	1.06	0.92	3.8	-35.1	98.9 (λ = 2190 nm)	250
$[Ge_{30}Se_{70}]_{1-x}[Sb]_x$				$Ge_{26}Sb_{13}Se_{61}$	1.77	1.54	2.77	12.2	23.5 (λ = 1320 nm)	300
				$Ge_{23}Sb_{22}Se_{55}$	1.44	1.27	3.03	42.5	45.4 (λ = 1620 nm)	250
				$Ge_{21}Sb_{30}Se_{49}$	1.2	1.03	3.3	11.7	78.8 (λ = 1930 nm)	250
$[Ge_{37}S_{63}]_{1-x-y}[Ge_{30}Se_{70}]_xSb_y$	$Ge_{37}S_{63}$			$Ge_{30}Sb_{11}S_{33}Se_{26}$	2.02	1.79	2.53	6.7	16.6 (λ = 1150 nm)	300
				$Ge_{28}Sb_{16}S_{31}Se_{25}$	1.82	1.59	2.67	10.7	22.4 (λ = 1270 nm)	300
				$Ge_{26}Sb_{22}S_{29}Se_{23}$	1.61	1.46	2.83	24.7	33.1 (λ = 1450 nm)	250
				$Ge_{24}Sb_{27}S_{28}Se_{21}$	1.42	1.37	2.96	45.3	50.6 (λ = 1640 nm)	250
				SiN_x	4.85	X	2.07	0.2	0.8 (λ = 480 nm)	>>400

Table 2. Summary of chalcogenide thin films obtained by (co-)sputtering deposition: composition, nature of the sputtering targets used for (co-)sputtering deposition, refractive index at 1.55 µm, band gap energy E_g^{04} and E_g^{CL}, n_2 Kerr nonlinear refractive index calculated either by means of the Sheik-Bahae model at 1.55 µm (n_2) and maximal n_2 values ($n_{2\,max}$) at energy near $0{,}534 \times E_g^{opt}$ eV (the corresponding wavelength value is also indicated into brackets) and a first evaluation of the limit temperature for material's stability (see text for details as well as "Methods" and Sect. 2 of the Supplementary Information).

Received: 6 June 2019; Accepted: 13 May 2020
Published online: 17 July 2020

References

1. Noé, P., Vallée, C., Hippert, F., Fillot, F. & Raty, J.-Y. Phase-change materials for non-volatile memory devices: From technological challenges to materials science issues. *Semicond. Sci. Technol.* **33**, 1 (2018).
2. Ovshinsky, S. R. Reversible electrical switching phenomena in disordered structures. *Phys. Rev. Lett.* **21**, 1450 (1968).
3. Verdy, A. *et al.* Improved electrical performance thanks to Sb and N doping in Se-rich GeSe-based OTS selector devices. *IEEE 9th Int. Mem. Work. , IMW* (2017).

4. Popescu, M. A. *Non Crystalline Chalcogenides* (Springer, Berlin, 2000).
5. Eggleton, B. J. *et al.* Chalcogenide photonics. *Nature Phot.* **5**, 141 (2011).
6. Tsiulyanu, D. & Ciobanu, M. Room temperature A.C. operating gas sensors based on quaternary chalcogenides. *Sensor. Actuat. B-Chem.* **223**, 95–100 (2016).
7. Lyubin, V., Klebanov, M., Feigel, A. & Sfez, B. Films of chalcogenide glassy semiconductors: New phenomena and new applications. *Thin Solid Films* **459**, 183–186 (2004).
8. Tanaka, K. Optical nonlinerity in photonic glasses. *J. Mater. Sci. Mater. Electron.* **16**, 633–643 (2005).
9. Mouawad, O. *et al.* Multioctave midinfrared supercontinuum generation in suspended-core chalcogenide fibers. *Opt. Lett.* **39**, 2684 (2014).
10. Petersen, C. R. *et al.* Mid-infrared supercontinuum covering the 1.4–13.3 μm molecular fingerprint region using ultra-high NA chalcogenide step-index fibre. *Nat. Phot.* **8**, 830–834 (2014).
11. Yu, Y. *et al.* Mid-infrared supercontinuum generation in chalcogenides. *Opt. Mat. Express* **3**, 1075 (2013).
12. Wang, H. *et al.* Compositional dependence of crystallization and structural stability in Ge-Sb-Se chalcogenide films. *J. Non-Cryst. Solids* **453**, 108–112 (2016).
13. Lin, L. *et al.* Photo-induced structural changes in Ge–Sb–Se films. *Infrared Phys. Techn.* **81**, 59–63 (2017).
14. Halenkovič, T. *et al.* Amorphous Ge–Sb–Se thin films fabricated by co-sputtering: Properties and photosensitivity. *J. Am. Ceram. Soc.* **101**, 1–13 (2018).
15. Petit, L. *et al.* Correlation between the nonlinear refractive index and structure of germanium-based chalcogenide glasses. *Mater. Res. Bull.* **42**, 2107–2116 (2007).
16. Sharma, N., Sharda, S., Sharma, V. & Sharma, P. Far-infrared investigation of ternary Ge–Se–Sb and quaternary Ge–Se–Sb–Te chalcogenide glasses. *J. Non-Cryst. Solids* **375**, 114–118 (2013).
17. Baudet, E. *et al.* Experimental design approach for deposition optimization of RF sputtered chalcogenide thin films devoted to environmental optical sensors. *Sci. Rep.* **7**, 3500 (2017).
18. Noé, P. *et al.* Impact of interfaces on scenario of crystallization of phase change materials. *Acta Mater.* **110**, 142–148 (2016).
19. Fillot, F. *et al.* Crystallization of $Ge_2Sb_2Te_5$ and nitrogren-doped $Ge_2Sb_2Te_5$ phase-change-materials thin films studied by in situ combined X-ray scattering techniques. *J. Appl. Crystallogr.* **51**, 1691–1705 (2018).
20. Smith, C., Jackson, J., Petit, L., Rivero-Baleine, C. & Richardson, K. Processing and characterization of new oxy-sulfo-telluride glasses in the Ge–Sb–Te–S–O system. *J. Solid stat. Chem.* **183**, 1891–1899 (2010).
21. Knotek, P. *et al.* Ageing of $Ge_{24.9}Sb_{11.6}S_{63.5}$ thin films under various conditions. *Mat. Chem. Phys.* **195**, 236–246 (2017).
22. Černošek, Z. *et al.* The properties and structure of Ge–Se–Te glasses and thin film. *J. Non-Cryst. Solids* **460**, 169–177 (2017).
23. Suriñach, S., Baró, M. D., Clavaguera-Mora, M. T. & Clavaguera, N. Glass forming ability and cristallization kinetics of allows in the $GeSe_2$-GeTe-Sb_2Te_3 system. *J. Non-Cryst. Solids* **111**, 113–119 (1989).
24. Olivier, M. *et al.* Photosensitivity of pulsed laser deposited Ge–Sb–Se thin films. *Opt. Mater. Express* **5**, 781–793 (2015).
25. Svoboda, R., Málek, J. & Liška, M. Correlation between the structure and relaxation dynamics of $(GeS_2)_y(Sb_2S_3)_{1-y}$ glassy matrices. *J. Non-Cryst. Solids* **479**, 113–119 (2018).
26. Yang, G. *et al.* Physical properties of the Ge_xSe_{1-x} glasses in the $0<x<0.42$ range in correlation with their structure. *J. Non-Cryst. Solids* **377**, 54–59 (2013).
27. Borisova, Z. *Glassy Semiconductors* (Springer, Berlin, 1981).
28. Tien, P. K., Ulrich, R. & Martin, R. J. Modes of propagating light waves in thin deposited semiconductor films. *Appl. Phys. Lett.* **14**, 291 (1969).
29. Sheik-Bahae, M., Hutchings, D. C., Hagan, D. J. & Van Stryland, E. W. Dispersion of bound electronic nonlinear refraction in solids. *J. Quantum Electron.* **27**, 1296–1308 (1991).
30. Boolchand, P., Grothaus, J., Tenhover, M., Hazle, M. A. & Grasselli, R. K. Structure of GeS2 glass: Spectroscopic evidence for broken chemical order. *Phys. Rev. B* **33**, 5421 (1986).
31. Gu, S., Zhang, Q. & Pan, R. Microstructure and mid-infrared refractive index dispersion of $Ge(S_xSe_{1-x})_4$ glasses. *Chalcogenide Lett.* **12**, 257–262 (2015).
32. Petit, L. *et al.* Effect of the substitution of S for Se on the structure of the glasses in the system $Ge_{0.23}Sb_{0.07}S_{0.70-x}Se_x$. *J. Phys. Chem. Solids* **66**, 1788–1794 (2005).
33. Dongol, M., Elhady, A. F., Ebied, M. S. & Abuelwafa, A. A. Impact of sulfur content on structural and optical properties of $Ge_{20}Se_{80-x}S_x$ chalcogenide glasses thin films. *Opt. Mat.* **78**, 266–272 (2018).
34. Griffiths, J. E., Espinosa, G. P., Phillips, J. C. & Remeika, J. P. Raman spectra and athermal laser annealing of $Ge(S_xSe_{1-x})_2$ glasses. *Phys. Rev. B* **28**, 4444–4453 (1983).
35. Xuecai, H., Guangying, S., Yu, L., Hongbo, Y. & Yonghua, L. Structure and vibrational modes of Ge–S–Se glasses: Raman scattering and ab initio calculations. *Chalcogenide Lett.* **9**, 465–474 (2012).
36. Noé, P. *et al.* Toward ultimate nonvolatile resistive memories: The mechanism behind ovonic threshold switching revealed. *Sci. Adv.* **6**, eaay2830 (2020).
37. Lee, J. H. *et al.* Unravelling interrelations between chemical composition and refractive index dispersion of infrared-transmitting chalcogenide glasses. *Sci. Rep.* **8**, 15482 (2018).
38. Olivier, M. *et al.* Wide-range transmitting chalcogenide films and development of micro-components for infrared integrated optics applications. *Opt. Mater. Express.* **4**, 525–540 (2014).
39. Pethes, I. *et al.* Atomic level structure of Ge-Sb-S glasses: Chemical short range order and long Sb–S bonds. *J. Alloy. Compd.* **774**, 1009–1016 (2019).
40. Watanabe, I. *et al.* Study on local structure in amorphous Sb–S films by Raman scattering. *J. Non-Cryst. Solids* **58**, 35–40 (1983).
41. Guery, G. *et al.* Evolution of glass properties during a substitution of S by Se in $Ge_{28}Sb_{12}S_{60-x}Se_x$ glass network. *J. Non-Cryst. Solids* **358**, 1740–1745 (2012).
42. d'Acapito, F. *et al.* Role of Sb dopant in Ag:GeS_x-based conducting bridge random access memories. *Phys. Status Solidi A* **213**, 311–315 (2016).
43. Upadhyay, M., Murugavel, S., Anbarasu, M. & Ravindran, T. R. Structural study on amorphous and crystalline state of phase change material. *J. Appl. Phys.* **110**, 083711 (2011).
44. Raty, J.-Y. Aging in phase change materials: Getting insight from simulation. *Phys. status solidi Rapid Res. Lett.* **1800590**, 1800590 (2019).
45. Klocek, P. & Colombo, L. Index of refraction, dispersion, bandgap and light scattering in GeSe and GeSbSe glasses. *J. Non-Cryst. Solids* **93**, 1–16 (1987).
46. Fang, Y. *et al.* Methods for determining the refractive indices and thermos-optic coefficients of chalcogenide glasses at MIR wavelengths. *Opt. Mater. X* **2**, 1000030 (2019).
47. Micoulaut, M. *et al.* Structure, topology, rings, and vibrational and electronic properties of Ge_xSe_{1-x} glasses across the rigidity transition: A numerical study. *Phys. Rev. B* **88**, 054203 (2013).
48. Munzar, M. *et al.* Some optical properties of Ge–S amorphous thin film. *Curr. Appl. Phys.* **2**, 181–185 (2002).
49. Tasseva, J., Lozanova, V. & Todorov, R. Linear and non-linear optical properties of GeS_2 doped with the elements from III and V group of the periodic table. *Bulg. Chem. Commun.* **45**, 33–37 (2013).
50. Raty, J.-Y. *et al.* Aging mechanisms in amorphous phase-change materials. *Nat. Commun.* **6**, 7467 (2015).

51. Ivanova, Z. G. *et al.* On the structural phase transformations in $Ge_xSb_{40-x}Se_{60}$ glasses. *J. Non-Cryst. Solids* **293–295**, 580–585 (2001).
52. Sharda, S., Sharma, N., Sharma, P. & Sharma, V. Band gap and dispersive behavior of Ge alloyed a-SbSe thin films using single transmission spectrum. *Mater. Chem. Phys.* **134**, 158–162 (2012).
53. Wang, T. *et al.* Systematic z-scan measurements of the third order nonlinearity of chalcogenide glasses. *Opt. Mater. Express* **4**, 1011–1022 (2014).
54. Pamukchieva, V., Szekeres, A., Sharlandjiev, P., Alexieva, Z. & Gartner, M. Effet of composition on refractive index dispersion in GeSbS thin films. *Proc. Int. Semiconduct. Con.* **1**, 101–104 (1998).
55. Fabian, M., Dulgheru, N., Antonova, K., Szekeres, A. & Gartner, M. Investigation of the atomic structure of Ge–Sb–Se chalcogenide glasses. *Adv. Condens. Matter Phys.* **2018**, 1–11 (2018).
56. Abdel-Wahab, F., Ali Karar, N. N., El Shaikh, H. A. & Salem, R. M. Effect of Sb on the optical properties of the Ge–Se chalcogenide thin films. *Phys. B* **422**, 40–46 (2013).
57. Shaaban, E. R., Kaid, M. A., El Sayed, M. & Adel, A. Effect of compositional variations on the optical properties of Sb–Ge–Se thin films. *J. Phys. D Appl. Phys.* **41**, 125301 (2008).
58. Shportko, K. *et al.* Resonant bonding in crystalline phase-change materials. *Nat. Mater.* **7**, 653–658 (2008).
59. Noé, P. & Hippert, F. Structure and properties of chalcogenide materials for PCM. In *Phase Change Memory* 125–179 (Springer, Cham, 2018).
60. Moss, T. S. A relationship between the refractive index and the infrared threshold of sensitivity for photoconductors. *Proc. Phys. Soc. Sect. B* **63**, 167–176 (1950).
61. Zakery, A. & Elliott, S. R. *Optical Nonlinearities in Chalcogenide Glasses and their Applications* (Springer, Berlin, 2007).
62. Wang, L. *et al.* Nonlinear silicon nitride waveguides based on a PECVD deposition platform. *Opt. Express* **26**, 9645–9654 (2018).
63. Choi, J. W., Chen, G. F. R., Ng, D. K. T., Ooi, K. J. A. & Tan, D. T. H. Wideband nonlinear spectral broadening in ultra-short ultra-silicon rich nitride waveguides. *Sci. Rep.* **6**, 27120 (2016).
64. Kuriakose, T. *et al.* Measurement of ultrafast optical Kerr effect of Ge-Sb-Se chalcogenide slab waveguides by the beam self-trapping technique. *Optics Comm.* **403**, 352–357 (2017).
65. Serna, S. *et al.* Nonlinear optical properties of integrated GeSbS chalcogenide waveguides. *Photon. Res.* **6**, B37–B42 (2018).
66. Chen, Y. *et al.* Optical and structure properties of amorphous Ge–Sb–Se films for ultrafast all-optical signal processing. *J. Alloy. Compd.* **580**, 578–583 (2013).
67. Romanova, E. *et al.* Measurement of non-linear optical coefficients of chalcogenide glasses near the fundamental absorption band edge. *J. Non-Cryst. Solids* **480**, 13–17 (2018).
68. Sugai, S. Stochastic random network model in Ge and Si chalcogenide glasses. *Phys. Rev. B* **35**, 1345–1361 (1987).
69. Fukunaga, T., Tanaka, Y. & Murase, K. Glass formation and vibration properties in the (Ge, Sn)-Se system. *Solid State Commun.* **42**, 513–516 (1982).
70. Jackson, K. *et al.* Raman-active modes of a-$GeSe_2$ and a-GeS_2: A first-principles study. *Phys. Rev. B* **60**, 14985–14989 (1999).
71. Lannin, J. S., Maley, N. & Kshirsagar, S. T. Raman scattering and short range order in amorphous germanium. *Solid State Commun.* **53**, 939–942 (1985).
72. Tao, H., Mao, S., Dong, G., Xiao, H. & Zhao, X. Raman scattering studies of the Ge-In sulphide glasses. *Solid State Commun.* **137**, 408–412 (2006).
73. Guo, H. T., Zhang, M.-J., Xu, Y.-T., Xia, X.-S. & Yang, Z.-Y. Structural evolution study of additions of Sb_2S_3 and CdS into GeS_2 chalcogenide glass by Raman spectroscopy. *Chin. Phys. B* **26**, 104208 (2017).
74. Lucovsky, G., Galeener, F. L., Keezer, R. C., Geils, R. H. & Six, H. A. Structural interpretation of the infrared and Raman spectra of glasses in the alloy system $Ge_{1-x}S_x$. *Phys. Rev. B* **10**, 5134–5146 (1974).
75. Lucovsky, G., Nemanich, R. J. & Solin, S. A. Coordination dependent vibrational properties of amorphous semiconductor alloys. *Solid State Commun.* **17**, 1567–1572 (1975).
76. Julien, C. *et al.* Raman and infrared spectroscopic studies of Ge–Ga–Ag sulphide glasses. *Mat. Sci. Eng. B* **22**, 191–200 (1994).
77. Quiroga, I. *et al.* Infrared studies of a $Ge_{0.20}Sb_{0.05}Se_{0.75}$ glassy semiconductor. *J. Non-Cryst. Solids* **196**, 183–186 (1996).
78. Petkov, K., Vassilev, G., Todorov, R., Tasseva, J. & Vassilev, V. Optical properties and structure of thin films from the system $GeSe_2$–Sb_2Se_3–AgI. *J. Non-Cryst. Solids* **357**, 2669–2674 (2011).
79. Lannin, J. S. Raman scattering properties of amorphous As and Sb. *Phys. Rev. B* **15**, 3863–3871 (1977).
80. Rossow, U. *et al.* Growth mode of ultrathin Sb layers on Si studied by spectroscopic ellipsometry and Raman scattering. *Appl. Surf. Sci.* **63**, 35–39 (1993).
81. Shakhvorostov, D. *et al.* Evidence for electronic gap-driven metal-semiconductor transition in phase-change materials. *PNAS* **106**, 10907–10911 (2009).
82. Lin, C. *et al.* Network structure in GeS_2-Sb_2S_3 chalcogenide glasses: Raman spectroscopy and phase transformation study. *J. Phys. Chem. C* **116**, 5862–5867 (2012).
83. Droichi, M. S., Vaillant, F., Bustarret, E. & Jousse, D. Study of localized states in amorphous chalcogenide Sb_2S_3 films. *J. Non-Cryst. Solids* **101**, 151–155 (1988).
84. Kamitsos, E. I., Kapoutsis, J. A., Culeac, I. P. & Iovu, M. S. Structure and bonding in As-Sb-S chalcogenide glasses by infrared reflectance spectroscopy. *J. Phys. Chem. B* **101**, 11061–11067 (1997).
85. Nazabal, V. *et al.* Sputtering and pulsed laser deposition for near- and mid-infrared applications: A comparative study of $Ge_{25}Sb_{10}S_{65}$ and $Ge_{25}Sb_{10}Se_{65}$ amorphous thin films. *J. Appl. Ceram. Technol.* **8**, 990–1000 (2011).
86. Raty, J.-Y. *et al.* Vibrational properties and stabilization mechanism of the amorphous phase of doped GeTe. *Phys. Rev. B* **88**, 014203 (2013).
87. Andrikopoulos, K. S., Yannopoulos, S. N., Kolobov, A. V., Fons, P. & Tominaga, J. Raman scattering study of GeTe and $Ge_2Sb_2Te_5$ phase-change materials. *J. Phys. Chem. Solids* **68**, 1074–1078 (2007).
88. Mendoza-Galvan, A., García-García, E., Vorobiev, Y. V. & González-Hernández, J. Structural, optical and electrical characterization of amorphous Se_xTe_{1-x} thin film alloys. *Microelectron. Eng.* **51–52**, 677–687 (2000).
89. Varma, G. S. *et al.* Thermally reversing window in $Ge_{15}Te_{85-x}In_x$ glasses: Nanoindentation and micro-Raman studies. *J. Non-Cryst. Solids* **358**, 3103–3108 (2012).
90. Uemura, O., Hayasaka, N., Tokairin, S. & Usuki, T. Local atomic arrangement in Ge–Te and Ge–S–Te glasses. *J. Non. Cryst. Solids* **205–207**, 189–193 (1996).
91. Brodsky, M. H., Gambino, R. J., Smith, J. E. & Yacoby, Y. The Raman spectrum of amorphous tellurium. *Phys. Stat. sol. B* **52**, 609 (1972).
92. Němec, P. *et al.* Amorphous and crystallized Ge–Sb–Te thin films deposited by pulsed laser: Local structure using Raman scattering spectroscopy. *Mater. Chem. Phys.* **136**, 935–941 (2012).
93. Hu, J. *et al.* Exploration of waveguide fabrication from thermally evaporated Ge–Sb–S glass films. *Opt. Mater.* **30**, 1560–1566 (2008).

Acknowledgements

E. Henaff is gratefully acknowledged for his availability and support during sputtering deposition of the chalcogenide thin films. We also sincerely acknowledge L. Duraffourg, head of the LCO laboratory of the DOPT department of CEA-LETI, for providing funding and related financial support for PhD thesis of J.-B. Dory. This

work has been partially supported by the EIPHI Graduate School (under contract"ANR-17-EURE-0002") and the FEDER Program of the Burgundy Region.

Author contributions

P.N. conceptualized and managed the project with help of C.S., B.C. and J.-B. J. J.-B. D. performed all experiments and treated all experimental data under supervision of P.N. and B.C. J.-B. D., C. C.-C., C.S., M.T. and M.B. prepared all the thin film samples in LETI clean rooms. J.-M. F. supported J.-B. D. for the supervision of the technological lots in LETI 200 mm technological platform. J.-B. D. performed spectroscopic ellipsometry data modelling under supervision of P.N., B.C. and A.C. J.-B.D. performed all Raman and FTIR experiments with invaluable help of A.V. The paper was written by J.-B. D. and P.N. with help of B.C. and A.V. All authors have given their approval to the final version of the manuscript.

Competing interests

The authors declare no competing interests.

Additional information

Supplementary information is available for this paper at https://doi.org/10.1038/s41598-020-67377-9.

Correspondence and requests for materials should be addressed to P.N.

Reprints and permissions information is available at www.nature.com/reprints.

Publisher's note Springer Nature remains neutral with regard to jurisdictional claims in published maps and institutional affiliations.

Open Access This article is licensed under a Creative Commons Attribution 4.0 International License, which permits use, sharing, adaptation, distribution and reproduction in any medium or format, as long as you give appropriate credit to the original author(s) and the source, provide a link to the Creative Commons license, and indicate if changes were made. The images or other third party material in this article are included in the article's Creative Commons license, unless indicated otherwise in a credit line to the material. If material is not included in the article's Creative Commons license and your intended use is not permitted by statutory regulation or exceeds the permitted use, you will need to obtain permission directly from the copyright holder. To view a copy of this license, visit http://creativecommons.org/licenses/by/4.0/.

© The Author(s) 2020